

# Sodium-Ion Hybrid Battery Combining an Anion-Intercalation Cathode with an Adsorption-Type Anode for Enhanced Rate and Cycling Performance

Jihui Lang<sup>+[a, b]</sup>, Jinrui Li<sup>+[a, b]</sup>, Fan Zhang<sup>+[a, b]</sup>, Xuan Ding,<sup>[b]</sup> Juan A. Zapien,\*<sup>[c]</sup> and Yongbing Tang<sup>\*[a, b]</sup>

Sodium-ion batteries (SIBs) are based on natural abundant and low-cost materials and show a good chemical safety. They have thus become an alternative battery technology to conventional lithium-ion batteries. However, SIBs usually suffer from poor rate capability and insufficient cycling performance caused by the sluggish reaction kinetics of the large Na<sup>+</sup> ions, restricting their practical application. Herein, we report a novel sodium-ion hybrid battery (SHB) combining an anion intercalation-type graphite cathode material with an adsorption-type hierarchical porous carbon anode material. The hierarchical porous amorphous carbon is derived from a natural biomass template with macro-, meso-, and micro-pores as well as high specific surface area, which are beneficial for fast adsorption/desorption of Na<sup>+</sup> ions. Consequently, attributed from the hybrid battery design, this SHB exhibits excellent rate capability and cycling performance with a reversible capacity of 80 mAh g<sup>-1</sup> at 2 C over a voltage window of 0–3.8 V and capacity retention of 87% after 1000 cycles at 10 C.

Exploiting rechargeable battery technologies with enhanced performance as well as low cost and environmental friendliness has become a global and urgent demand since the explosive growth of portable electronic devices, electric vehicles as well as large-scale energy storage.<sup>[1–18]</sup> Meanwhile, the limited and uneven distribution of lithium resource has stimulated extensive investigations of energy storage devices based on other abundant metal ions, such as Na<sup>+</sup>,<sup>[12–25]</sup> K<sup>+</sup>,<sup>[26–30]</sup> Al<sup>3+</sup>,<sup>[31,32]</sup> etc. Among them, sodium-ion batteries (SIBs) have attracted increased attention owing to the merits of low potential

(−2.71 V vs. standard hydrogen electrode (SHE)), high natural abundance, low cost, and similar electrochemical properties to lithium.<sup>[19–21]</sup> Nevertheless, the larger size of Na<sup>+</sup> (0.98 Å) than Li<sup>+</sup> (0.69 Å)<sup>[22]</sup> results in sluggish diffusion kinetics and the following unsatisfied rate capability and cycling performance. While many efforts have been focused on designing appropriate electrode cathode or anode materials with optimized structures to solve the above issues,<sup>[23–25]</sup> new battery construction design could also be another suitable strategy.

To accelerate the ion diffusion kinetics in the cathode in SIBs, an unexpected way is introducing graphitic carbon with redox amphotericity as cathode material, which has been demonstrated that anion intercalation/deintercalation into/from graphite layer shows intrinsic fast diffusion behavior in dual-ion batteries.<sup>[33–45]</sup> On the other hand, to improve the Na<sup>+</sup> diffusion kinetics in the anode, other than using conventional battery-type materials, a simple and efficient way is employing capacitive-type material, which not only exhibits fast kinetics but also shows excellent structural stability. Therefore, it is promising to achieve both high rate performance and long cycling life for SIBs by combining anion intercalation with Na<sup>+</sup> adsorption mechanism together.

Herein, we firstly construct a novel sodium-ion hybrid battery (SHB) by introducing an anion intercalation-type mesocarbon microbead (MCMB) as cathode material and an adsorption-type material, hierarchical porous amorphous carbon (HPAC) as anode material. The prepared HPAC exhibited a porous architecture with hierarchical macro-, meso-, and micro-pores and a high specific surface area of 3100 m<sup>2</sup> g<sup>-1</sup> with large cumulative pore volume of 1.33 cm<sup>3</sup> g<sup>-1</sup>, which is beneficial for improving the reaction kinetics of adsorption/desorption of Na<sup>+</sup> ions. Moreover, by combining the fast anion intercalation-type cathode and capacitive-type anode together, the present SHB achieves both excellent rate capability and good cycling performance, with a reversible capacity of 80 mAh g<sup>-1</sup> at 2 C and capacity retention of 87% after 1000 cycles at 10 C.

Figure 1 schematically illustrates the configuration and the working mechanism of the SHB. The HPAC is designed as anode material, MCMB is used as cathode material, meanwhile 1 M NaPF<sub>6</sub>/EC-DMC-EMC (1:1:1 v/v/v) is used as the electrolyte. During the charging state, PF<sub>6</sub><sup>-</sup> anions intercalate into the graphitic layer in the MCMB cathode, meanwhile Na<sup>+</sup> cations are adsorbed into the micro/mesopores in the HPAC anode. During the discharging state, Na<sup>+</sup> and PF<sub>6</sub><sup>-</sup> are desorbed/deintercalated from the anode and cathode respectively and move back to the electrolyte. As the HPAC anode shows a fast

[a] Prof. J. Lang,\* J. Li,<sup>+</sup> Dr. F. Zhang,<sup>+</sup> Prof. Y. Tang  
Key Laboratory of Functional Materials Physics and Chemistry of the Ministry of Education  
Jilin Normal University  
Siping 136000, China  
E-mail: tangyb@sjat.ac.cn

[b] Prof. J. Lang,<sup>+</sup> J. Li,<sup>+</sup> Dr. F. Zhang,<sup>+</sup> X. Ding, Prof. Y. Tang  
Functional Thin Films Research Center  
Shenzhen Institutes of Advanced Technology  
Chinese Academy of Sciences  
Shenzhen, 518055, China

[c] Prof. J. A. Zapien  
Center of Super-Diamond and Advanced Film (COSDAF)  
City University of Hong Kong  
Hong Kong SAR, China  
E-mail: apjazs@cityu.edu.hk

[+] J. H. Lang, J.R. Li, and F. Zhang contributed equally to this work.

 Supporting information for this article is available on the WWW under <https://doi.org/10.1002/batt.201800138>

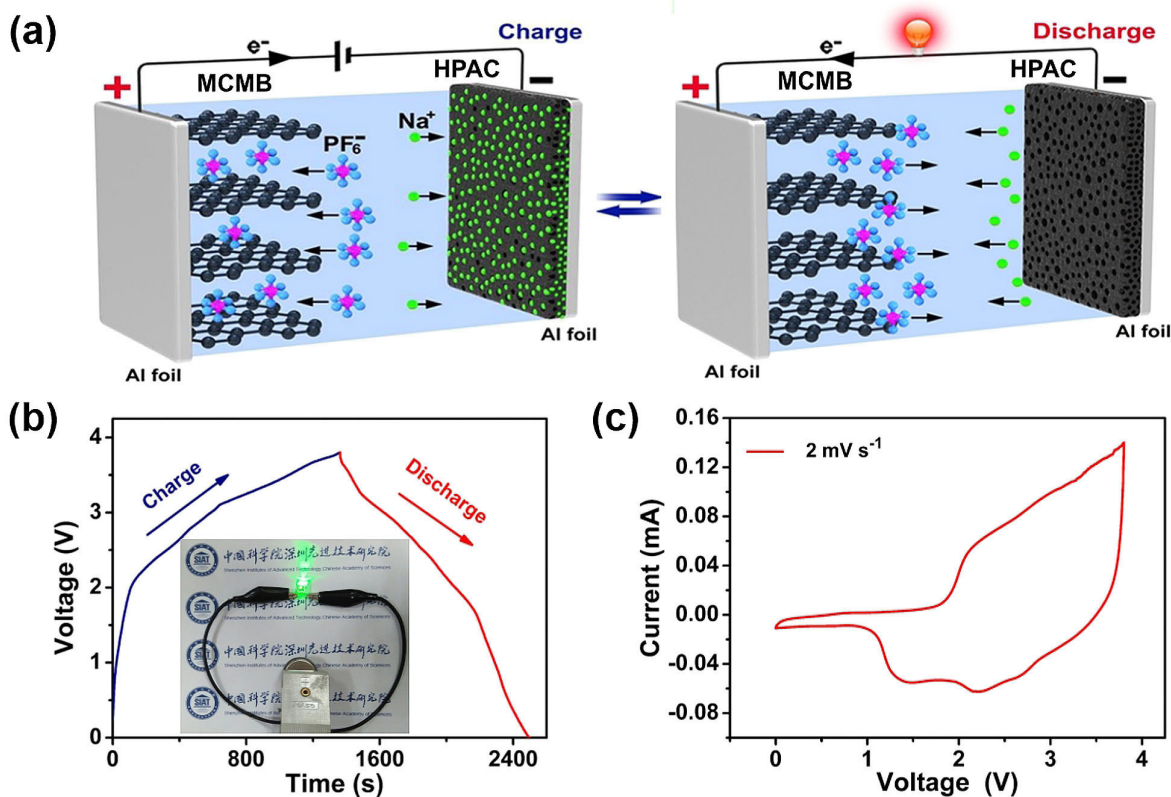


**Figure 1.** a) Schematic illustration of the battery configuration and charging/discharging process of the SHB based on HPAC anode and MCMB cathode. b) Charge-discharge curves of the SHB at a current density of 2 C in the voltage window of 0–3.8 V. c) CV curve of the SHB at a scan rate of  $2 \text{ mV s}^{-1}$ .

cation adsorption/desorption process during charging/discharging, the polarization variation of the SHB is mainly determined by the MCMB cathode. Anion intercalation/deintercalation into graphite cathode typically displays a low voltage hysteresis between charge and discharge, thus results in high voltage efficiency and energy efficiency, especially at low current rates.<sup>[46]</sup> Figure 1b shows the typical charge-discharge curves of the SHB at a current density of 2 C (1 C =  $100 \text{ mA g}^{-1}$ ) in the voltage window of 0–3.8 V. The charge-discharge slopes of the SHB are non-ideal linear, indicating hybrid reaction mechanisms. Inset of Figure 1b shows that one SHB coin cell can light up a green LED owing to the high voltage window. Figure 1c shows the cyclic voltammetry (CV) curve of the SHB at a scan rate of  $2 \text{ mV s}^{-1}$ , which displays redox regions located at around 1.8–3.8 V and 3.8–1.0 V, indicating a combination of intercalation/deintercalation of  $PF_6^-$  on graphite cathode (Figure S1)<sup>[42]</sup> and  $Na^+$  adsorption/desorption on HPAC anode.

To obtain the best performance of the SHB, various HPAC materials were prepared by optimizing the activation process. Figure 2a shows the schematic figure of the preparation process of HPAC. As has been pointed out by Armand et al., utilization of natural materials to provide sustainable power will be the trend of future development of energy storage devices.<sup>[47]</sup> Lotus root was chosen as the bio-template of porous carbon owing to its intrinsic porous structure. After freeze drying, carbonization, and activation, hierarchical porous

amorphous carbon can be formed. During the activation process, HPAC materials with different carbide/KOH weight ratios (1:2, 1:3, 1:4, and 1:5) were prepared and named as HPAC2, HPAC3, HPAC4, and HPAC5 respectively. Scanning electron microscope (SEM) image in Figure 2b shows that the lotus root precursor has a honeycomb-like macroporous structure, which is beneficial for homogenous impregnation of KOH during activation to form hierarchical meso-/micropores. Figure 2c,d show SEM images of a typical activated product HPAC with different magnifications, revealing its 3D hierarchical porous structure with macropores and meso-/micropores full-filled in the skeleton of HPAC4. Figure 2e further demonstrates its microstructure by high-resolution transmission electron microscope (HRTEM), which exhibits highly meso-/microporous structure with pore size of  $1\text{--}3 \text{ nm}$ , surrounded by highly curved carbon nanosheets. The X-ray diffraction (XRD) patterns of the prepared samples (Figure 2f) show low and wide peaks with no obvious sharp peaks, indicating their amorphous structure caused by numerous micro/mesopores. The Raman spectra of the HPACs and YP50 clearly display two characteristic peaks at  $\sim 1350 \text{ cm}^{-1}$  (D-band) and  $\sim 1580 \text{ cm}^{-1}$  (G-band) (Figure 2g), and the  $I_D/I_G$  of HPAC4 shows the highest value of 4.582, indicating that HPAC4 has the highest ratio of defects and smallest crystalline size.<sup>[48]</sup>

The  $N_2$  adsorption measurement confirms the porous structure of the HPAC materials (Figure 3a), which can be seen that the adsorbed amount of HPAC increases with the increase

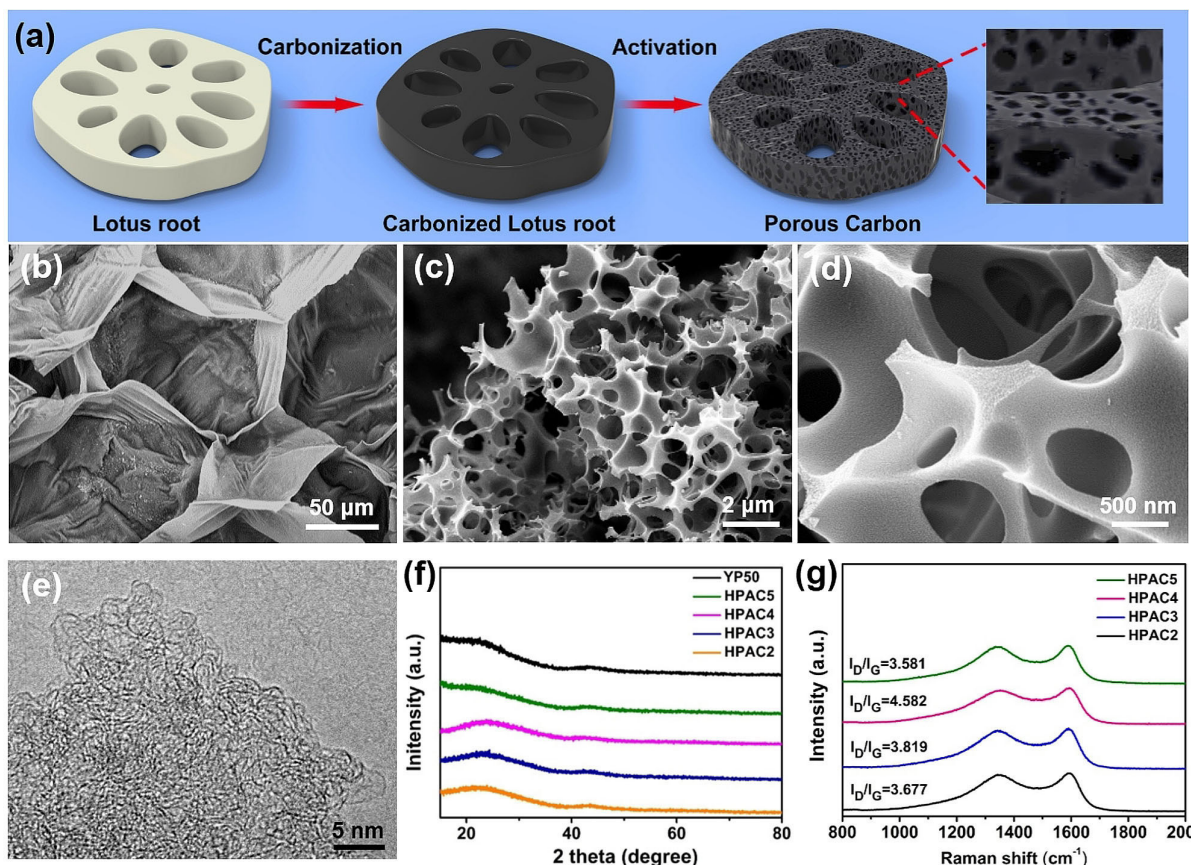


**Figure 2.** a) Schematic of the fabrication process of the HPAC material. b) SEM images of lotus root aerogel. b), c) SEM images of the activated product HPAC4 with different magnifications. e) HRTEM image of the HPAC4. f) XRD patterns of different HPAC materials and commercial activated carbon YP50 as contrast. g) Raman spectra of different HPAC materials and commercial activated carbon YP50 as contrast.

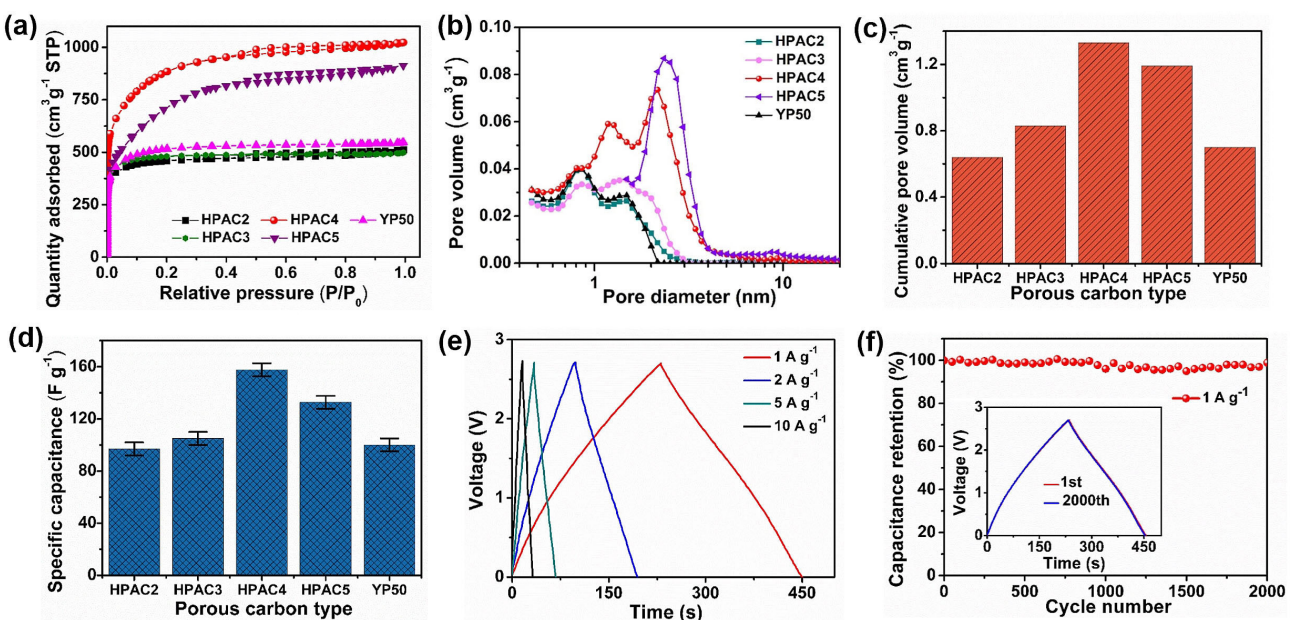


**Figure 3.** a) N<sub>2</sub> adsorption-desorption isotherms, b) pore size distribution, and c) cumulative pore volume of the HPAC2, HPAC3, HPAC4, HPAC5 and commercial activated carbon YP50 as contrast. d) Specific capacitance of the HPAC2, HPAC3, HPAC4, HPAC5, and YP50 as contrast. e) Charge-discharge curves of the HPAC4-based supercapacitor at current density of 1, 2, 5, and 10 A g<sup>-1</sup>. f) Long cycling stability of the HPAC4-based supercapacitor for 2000 cycles at 1 A g<sup>-1</sup>. Inset is the charge-discharge curves of the HPAC4-based supercapacitor in the 1st and 2000th cycle.

of KOH amount from 2 to 4 times. In addition, the HPAC4 and HPAC5 exhibit type IV characteristic adsorption/desorption curves, indicating mesoporous structure. The HPAC5 has lower adsorption amount than HPAC4, which may be due to the collapse of micropores caused by excessive KOH activation. Brunauer-Emmett-Teller (BET) specific surface areas (SSAs) of HPAC2, HPAC3, HPAC4, HPAC5 and commercial activated carbon YP50 were calculated to be 1776, 1969, 3107, 2471, and  $1953\text{ m}^2\text{ g}^{-1}$  (Figure S2). The corresponding pore size distribution (PSD) analysis (Figure 3 b) demonstrates that HPAC2 and HPAC3 prepared with lower KOH addition mainly possess micropores below 2 nm, while the PSD of the HPAC4 shifts towards mesopores centered around 1–4 nm, and the HPAC5 with the largest KOH addition mainly obtains mesopores. Figure 3c further reveals that the HPAC4 has the largest cumulative pore volume of  $1.33\text{ cm}^3\text{ g}^{-1}$ , indicating the largest adsorption/desorption of  $\text{Na}^+$  ions in full battery.

To evaluate the capacitance behavior of the HPACs, symmetric supercapacitors were fabricated with resulting electrochemical performance as shown in Figure 3d-f. The specific capacitance of the HPAC2, HPAC3, HPAC4, HPAC5 and YP50 obtained by galvanostatic test under  $1\text{ A g}^{-1}$  is 97, 105, 158, 133, and  $100\text{ F g}^{-1}$  respectively (Figure 3d), which is proportional to the SSA results. The cyclic voltammetry (CV) curves of the HPAC4 electrode at different scan rates (Figure S3), show rectangular-shape curves at 10, 20, and  $50\text{ mV s}^{-1}$ , revealing electronic double layer capacitive (EDLC) behavior. The charge-discharge curves present nearly equicrural triangle lines (Figure 3e) at different current densities from 1 to  $10\text{ A g}^{-1}$ , and the specific capacitance remains at 156, 142, 135 and  $128\text{ F g}^{-1}$  at current density of 1, 2, 5, and  $10\text{ A g}^{-1}$  respectively, illustrating standard capacitive behavior and good rate performance of the HPAC-based supercapacitor. Furthermore, the HPAC4 also exhibits excellent cycling stability with nearly 100% capacitance retention after 2000 cycles under  $1\text{ A g}^{-1}$  as presented in Figure 3f.

Given the excellent capacitive performance of HPAC4, we further designed a sodium-ion hybrid battery (SHB) by using HPAC4 as anode material and MCMB as cathode material in a  $\text{NaPF}_6$ -containing carbonate electrolyte. To demonstrate the working mechanism, structural characterizations of the MCMB cathode and HPAC4 anode were performed. XRD patterns of the MCMB cathode with initial, charging, and discharging states are shown in Figure 4a. Obviously, a sharp diffraction peak of pristine MCMB appears at  $26.8^\circ$  corresponding to (002) plane, indicating high crystallinity of MCMB. When the charging process proceeds, the (002) peak of the MCMB cathode gradually splits into two weak peaks accompanying with the deflection to lower angle, indicating the  $\text{PF}_6^-$  intercalation process.<sup>[49–51]</sup> When fully charged, the (002) peak completely shifts to  $25^\circ$ , indicating a complete intercalation process. Conversely, during the discharging process, the two split peaks gradually merge into one broad peak at  $26^\circ$ . However, the position and the intensity of the (002) peak cannot recover its initial value even after fully discharged, which is attributed to the partially irreversible deintercalation of the  $\text{PF}_6^-$  anions from the graphitic layer in the first cycle. The  $\text{PF}_6^-$  intercalation/de-

intercalation process into/from the MCMB was also proved by ex-situ Raman spectra (Figure 4a) during the first charge-discharge cycle. At the charging state, the G band located at  $1584\text{ cm}^{-1}$  gradually diminished and split into two peaks, corresponding to  $E_{2g2}(i)$  and  $E_{2g2}(b)$  mode.<sup>[42,52]</sup> The peak for  $E_{2g2}(i)$  migrates to  $1587\text{ cm}^{-1}$  while the peak for  $E_{2g2}(b)$  migrates to  $1608\text{ cm}^{-1}$  in the fully charged state. Conversely, during the discharge process, the  $E_{2g2}(i)$  and  $E_{2g2}(b)$  peaks gradually merged into one peak until recovering its initial state thus confirming the  $\text{PF}_6^-$  intercalation/deintercalation process.

Next, we investigate the adsorption/desorption process of the HPAC4 anode, X-ray photoelectron spectroscopy (XPS) analysis on the HPAC4 anode at fully charged and discharged state. As shown in Figure 4b, the Na 1s characteristic peak is located at the  $1071.4\text{ eV}$  in the fully charged state; whereas, in the fully discharged state, this peak is non-visible. Figure 4c further shows the C 1s peaks at  $284.6$ ,  $284.7$ ,  $284.8$ ,  $286.8$  and  $290.7\text{ eV}$  corresponding to  $\text{C}=\text{C}$ ,  $\text{C}-\text{C}$ ,  $\text{C}-\text{O}$ ,  $\text{C}=\text{O}$ , and  $\text{O}-\text{C}=\text{O}$  respectively at the charging state. After fully discharging, the peaks show little change with no obvious shift. Energy dispersive X-ray spectroscopy (EDX) mapping analysis of the HPAC4 anode (Figure 4d,e) also displays obvious and uniform Na element signal with  $\sim 11\text{ at\%}$  in the fully charged state, while at fully discharged state the Na content decreased to  $\sim 0\text{ at\%}$ . All the above results indicate physical and reversible adsorption/desorption process of  $\text{Na}^+$  on the HPAC4 anode.

The electrochemical performance of the MCMB//HPAC4 SHB was then investigated in the voltage window of  $0$ – $3.8\text{ V}$ . CV curves at different scan rates (Figure 5a) were investigated to analyze the kinetics process of the SHB according to the formula  $i=av^b$  ( $i$  is the peak current and  $v$  is the scan rate).<sup>[53–55]</sup> The  $b$  values (Figure 5b) of the cathodic peak and anodic peak of the SHB were calculated to be 0.75 and 0.65 respectively, which are between 1.0 (fully capacitive behavior) and 0.5 (fully diffusion controlled), indicating the contribution from both diffusion-controlled process and surface capacitive behavior.

Figure 5c presents charge-discharge profiles of the SHB at different current rates from  $2\text{ C}$  to  $10\text{ C}$ . All the charge-discharge curves of the SHB at different current rates show with no obvious voltage plateaus nor straight slopes, indicating a combination of the intercalation mechanism and adsorption mechanism. It is clearly seen that the SHB can operate normally for over  $380\text{ s}$  to  $2500\text{ s}$  with stable charge-discharge curves in similar shapes, and the specific capacity of the SHB is  $80$ ,  $74$ ,  $70$ ,  $67$ , and  $59\text{ mAh g}^{-1}$  at  $2\text{ C}$ ,  $3\text{ C}$ ,  $4\text{ C}$ ,  $5\text{ C}$ , and  $10\text{ C}$  respectively (Figure 5d), demonstrates its good rate performance. Furthermore, the SHB also exhibits stable cycling performance with 90% capacity retention after 1000 cycles at  $10\text{ C}$  (Figure 5e). The morphology (Figures S4, S5) and XRD profiles (Figure S6) of the HPAC4 anode and MCMB cathode show no obvious changes after long cycles, except for a little peak shift of MCMB due to partially irreversible  $\text{PF}_6^-$  intercalation, thus indicating good structural stability of the materials. In addition, the charge-discharge curves of the SHB for the 1st, 200th, 500th, and 1000th cycle (Figure S7a) show slight capacity loss and good stability. Figure S7b shows the electrochemical impedance spectroscopy (EIS) tests of the SHB after different number

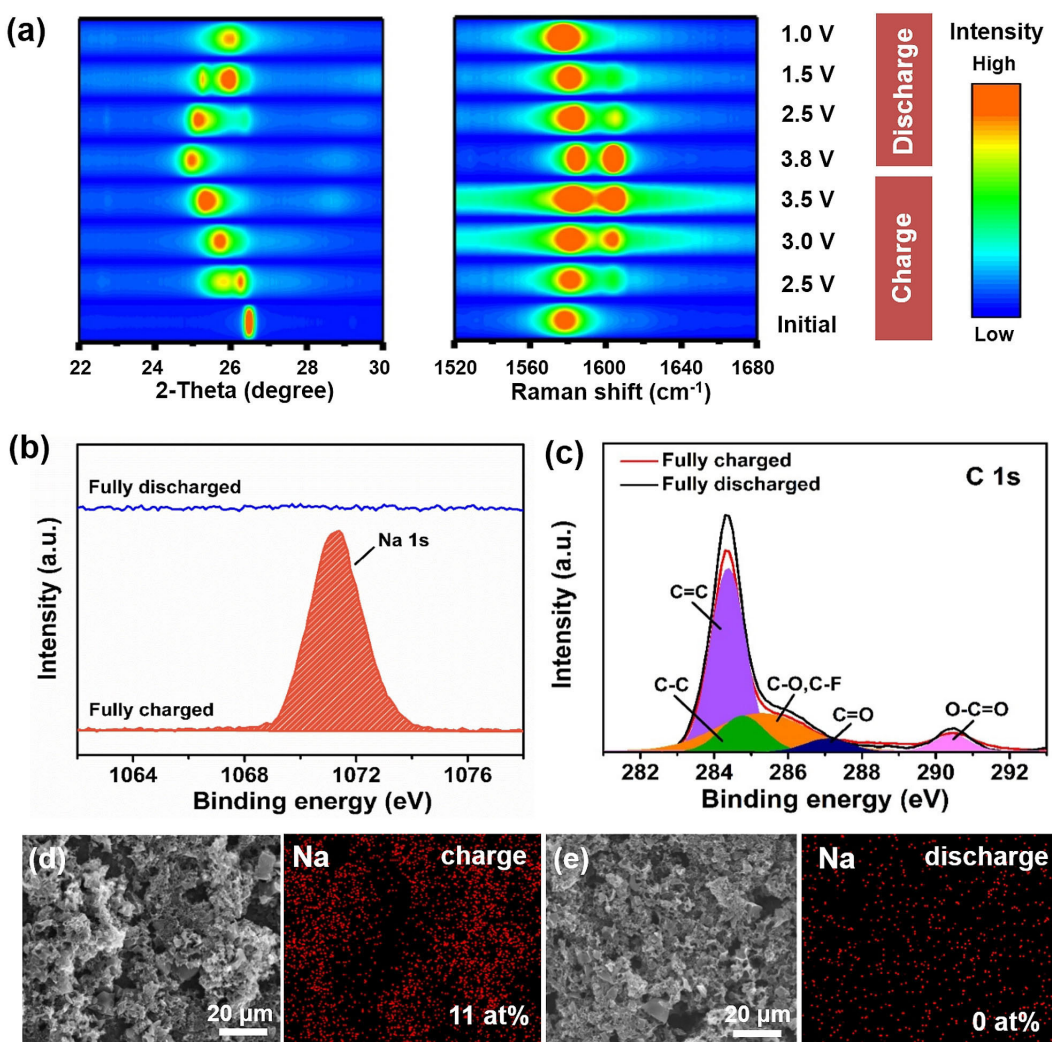


**Figure 4.** a) Ex-situ XRD patterns and Raman spectra of the MCMB cathode at different charging/discharging states. b), c) XPS spectra of the Na 1s (c) and C 1s (d) of the HPAC4 anode at fully charged and fully discharged state. d), e) EDX mapping images of Na element on the HPAC4 anode at fully charged state (d) and fully discharged state (e).

of cycles. It is clearly seen that after 10 cycles, the diameter of the depressed semicircle at high-to-middle frequency (corresponding to charge transfer resistance,  $R_{ct}$  value) becomes smaller and remains stable for over 150 cycles, implying an electrochemical activation process during initial cycles, as well as fast and stable electrochemical kinetics in the following cycles. The energy density and power density of the SHB based on the total mass of electrodes were further estimated. The SHB delivers a gravimetric energy density of 60 Wh kg<sup>-1</sup> with a power density of 1500 W kg<sup>-1</sup> (Table S1), and a volumetric energy density of 53 Wh L<sup>-1</sup> with a power density of 161 WL<sup>-1</sup>, which are between those of batteries and supercapacitors owing to a combined mechanism of intercalation and absorption,<sup>[56]</sup> and comparable with reported hybrid capacitors.<sup>[57-61]</sup> Therefore, the high rate capability, long cycling life and low cost of the SHB make it promising for large energy storage applications.

In summary, we have developed a new sodium-ion hybrid battery configuration by combining an anion-intercalation type

MCMB cathode an adsorption-type material namely hierarchical porous amorphous carbon (HPAC) anode using lotus root as precursor via a freeze-drying, carbonization and activation method. The HPAC exhibits both high specific surface area and hierarchical porous structure with macro-, meso-, and micro-pores, contributing to high capacitance as well as fast and stable electrochemical kinetics. Therefore, the SHB exhibits both excellent rate capability and long cycling performance with 80 mAh g<sup>-1</sup> at 2 C and capacity retention of 87% after 1000 cycles at 10 C. Moreover, the hybrid battery design with high performance opens a new avenue for developing high-performance and low-cost energy storage systems.

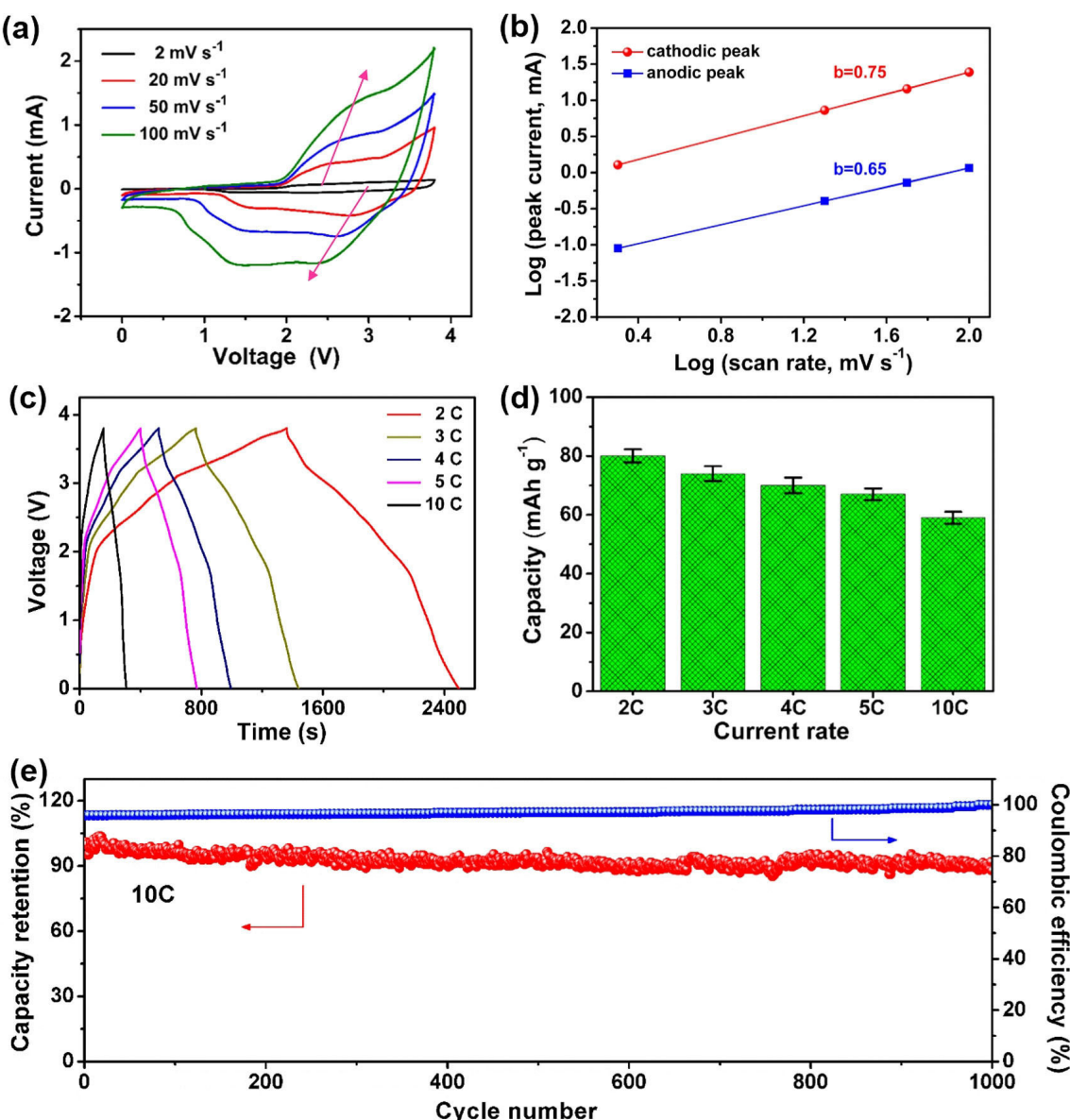


**Figure 5.** a) CV curves of the SHB at different scan rates of 2, 20, 50, and 100 mV s<sup>-1</sup>. b) Calculation of  $b$ -values by the relationship of the scan rate and peak current. c) Charge-discharge curves of the SHB at different current rates of 2, 3, 4, 5, and 10 C. d) Corresponding specific capacities of the SHB at different current rates. e) Long cycling performance of the SHB for 1000 cycles at 10 C.

## Experimental Section

### Materials

Meso-carbon microbead (MCMB), acetylene black, polyvinylidene fluoride (PVDF), and N-methyl-2-pyrrolidone (NMP) were bought from Shenzhen Kejingstar Technology Ltd. Glass fiber separator (Whatman, 0.5 mm) was bought from Shanghai Huanao Technology Ltd. NaPF<sub>6</sub> (99.5%), ethylene carbonate (EC, 99.95%), dimethyl carbonate (DMC, 99.95%) and ethyl methyl carbonate (EMC, 99.95%) were purchased from Dodochem. The electrolyte was home-made and the composition is 1 M NaPF<sub>6</sub> in EC-DMC-EMC (1:1:1 v/v/v).

### Preparation of Hierarchical Porous Amorphous Carbon (HPAC)

The HPAC material was synthesized as follows. First, lotus root was washed with de-ionized water and freeze-dried for 72 h, and then carbonized in 800 °C for 2 h under an atmosphere of argon in a tube furnace. Next, the prepared sample was mixed uniformly with KOH powder by different ratios in a mortar and the mixture was annealed at 800 °C for 1 h under Ar in a tube furnace with a heating rate of 5 °C min<sup>-1</sup>. Finally, the product was washed by 0.1 M HCl and de-ionized water for several times until pH = 7 and dried at 80 °C in vacuum for 12 h. Based on the different carbide/KOH weight ratios of 1:2, 1:3, 1:4, and 1:5, the products were named as HPAC2, HPAC3, HPAC4, and HPAC5 respectively.

## Characterization

The morphology of the materials and electrodes were analyzed by field-emission scanning electron microscope (FE-SEM, HITACHI S-4800) and transmission electron microscope (TEM, JEOL JEM-3200FS). N<sub>2</sub> physical adsorption-desorption analysis was tested on an instrument ASAP 2020HD88 (American). Ex-situ X-ray diffraction (XRD) analyses was carried out by using Rigaku D/Max-2500 diffractometer (Japan) operated at 40 kV and 100 mA (Cu K $\alpha$  radiation). Ex-situ Raman spectra analyses of MCMB cathode were recorded on a LabRAM HR Raman spectrometer (633 nm) at different charging/discharging states in the frequency range of 1500–1700 cm<sup>-1</sup>. X-ray photoelectron spectroscopy (XPS) (ESCALAB 250Xi, Thermo Fisher) as measured with monochromatic aluminum K $\alpha$  radiation. All the electrodes for the ex-situ XRD, Raman and XPS tests were washed by DMC and dried in the glove box.

## Electrochemical Characterization

For preparing the HPAC anode, homogeneous slurry was made by mixing 80 wt% HPAC, 10 wt% acetylene black, and 10 wt% PVDF and several drops of NMP solvent together and then dried at 80 °C in vacuum for 12 h, which was then coated onto carbon-coated Al foil. The MCMB cathode was prepared by a similar method. The HPAC anode, MCMB cathode, and glass fiber were punched into circular sheets with diameters of 1.2, 1.0, and 1.6 cm respectively, and then assembled to form CR2032 coin cell in an Ar-filled glove box (MIKROUNA) with 1 M NaPF<sub>6</sub>/EC-DMC-EMC (1:1:1 v/v/v) as electrolyte for electrochemical test. Galvanostatic charge-discharge measurements of the battery was tested on a battery test system (LAND CT2001A). Electrochemical impedance spectroscopy (EIS) and cyclic voltammetry (CV) measurements was performed on an Autolab (PGSTAT302N, Switzerland) electrochemical workstation.

### Calculation of Energy Density and Power Density of the SHB

#### (1) Calculation of gravimetric energy density of the SHB

In the SHB system, the mass ratio of MCMB cathode ( $m_c$ ) and HPAC4 anode ( $m_a$ ) is around 1:1. The gravimetric energy density based on the MCMB cathode ( $E_c$ ) is 172 Wh kg<sup>-1</sup> at 2 C obtained from the battery test system, thus the gravimetric energy density based on both cathode and anode ( $E_{c+a}$ ) is 86 Wh kg<sup>-1</sup>.

#### (2) Calculation of volumetric energy density of the SHB

The volumetric energy density of the SHB based on both cathode and anode materials is calculated to be around 53 Wh L<sup>-1</sup> at 2 C, and the calculation formula is as follows (the tap density of MCMB cathode and HPAC4 anode is 2.20 and 0.36 g cm<sup>-3</sup> respectively):

$$E_v = \frac{E_c \times m_c}{V_c + V_a} = E_c \times \frac{m_c/V_c}{(V_c + V_a)/V_c} = E_c \times \frac{\rho_c}{1 + \frac{m_a}{\rho_a} \times \frac{\rho_c}{m_c}}$$

$$= 172 \times \frac{2.20}{1 + 1 \times \frac{2.20}{0.36}} = 53 \text{ Wh L}^{-1}$$

#### (3) Calculation of gravimetric and volumetric power density of the SHB

The power density of the SHB is calculated by the following formula  $P = E/t$ .

## Acknowledgements

The authors gratefully acknowledge financial support from the National Natural Science Foundation of China (No. 51822210), Shenzhen Peacock Plan (KQJSCX20170331161244761 and KQTD2016112915051055), Natural Science Foundation of Guangdong Province (Grant No. 2017A030310482), Shenzhen Science and Technology Planning Project (JSGG20170413153302942, JCYJ20170307171232348, JCYJ20170818160918762, JCYJ20170818153427106, JCYJ20170818153404696 and JCYJ20170818153339619, JCYJ20160229165250876), and Scientific Project of Chinese Academy of Sciences (KFJ-STS-SCYD-124).

## Conflict of Interest

The authors declare no conflict of interest.

**Keywords:** Adsorption • anion-intercalation • hierarchical porous carbon • hybrid batteries • sodium-ion batteries

- [1] A. M. Navarro-Suárez, K. Maleski, T. Makaryan, J. Yan, B. Anasori, Y. Gogotsi, *Batteries* **2018**, *1*, 33–38.
- [2] S. N. S. Hapuarachchi, J. Y. Nerkar, K. C. Wasalathilake, H. Chen, S. Zhang, A. P. O'Mullane, C. Yan, *Batteries* **2018**, *1*, 122–128.
- [3] Q. Sun, K. C. Lau, D. Geng, X. Meng, *Batteries* **2018**, *1*, 41–68.
- [4] J. Liang, F. Li, H.-M. Cheng, *Energy Storage Mater.* **2017**, *7*, A1–A3.
- [5] M. Zhang, X. H. Song, X. W. Ou, Y. B. Tang, *Energy Storage Mater.* **2019**, *16*, 65–84.
- [6] C. Chen, X. Xie, B. Anasori, A. Sarycheva, T. Makaryan, M. Zhao, P. Urbankowski, L. Miao, J. Jiang, Y. Gogotsi, *Angew. Chem. Int. Ed.* **2018**, *57*, 1846–1850; *Angew. Chem.* **2018**, *130*, 1864–1868.
- [7] B. Breitung, A. Schneider, V. S. K. Chakravadhanula, C. Suchomski, J. Janek, H. Sommer, T. Brezesinski, *Batteries* **2018**, *1*, 27–32.
- [8] H. Wang, M. Wang, Y. B. Tang, *Energy Storage Mater.* **2018**, *13*, 1–7.
- [9] M. Widmaier, K. Pfeifer, L. Bommer, V. Presser, *Batteries* **2018**, *1*, 11–26.
- [10] M. Wang, F. Zhang, C. S. Lee, Y. B. Tang, *Adv. Energy Mater.* **2017**, *7*, 1700536.
- [11] Q. Liu, Z. Chang, Z. Li, X. Zhang, *Small Methods* **2018**, *2*, 1700231.
- [12] B. F. Ji, F. Zhang, M. H. Sheng, X. F. Tong, Y. B. Tang, *Adv. Mater.* **2017**, *29*, 1604219.
- [13] Y. Xiao, D. Su, X. Wang, S. Wu, L. Zhou, Y. Shi, S. Fang, H.-M. Cheng, F. Li, *Adv. Energy Mater.* **2018**, *8*, 1800930.
- [14] Y. Fang, X.-Y. Yu, X. W. Lou, *Angew. Chem. Int. Ed.* **2017**, *56*, 5801–5805; *Angew. Chem.* **2017**, *129*, 5895–5899.
- [15] C. L. Jiang, Y. Fang, W. Y. Zhang, X. H. Song, J. H. Lang, L. Shi, Y. B. Tang, *Angew. Chem. Int. Ed.* **2018**, *57*, 1810575.
- [16] M. Krengel, A.-L. Hansen, F. Hartmann, J. V. Dinter, W. Bensch, *Batteries* **2018**, *1*, 176–183.
- [17] C. Zhao, Y. Lu, Y. Li, L. Jiang, X. Rong, Y.-S. Hu, H. Li, L. Chen, *Small Methods* **2017**, *1*, 1600063.
- [18] E. Wang, M. Chen, X. Liu, Y. Liu, H. Guo, Z. Wu, W. Xiang, B. Zhong, X. Guo, S. Chou, S.-X. Dou, *Small Methods* **2018**, *2*, 1800169.
- [19] D. Werner D. H. Apaydin, E. Portenkirchner, *Batteries* **2018**, *1*, 160–168.
- [20] X. Sun, W. Li, X. Zhong, Y. Yu, *Energy Storage Mater.* **2017**, *9*, 112–118.
- [21] M. Sheng, F. Zhang, B. Ji, X. Tong, Y. B. Tang, *Adv. Energy Mater.* **2017**, *7*, 1601963.
- [22] M. Arnaiz, P. Huang, J. Ajuria, T. Rojo, E. Goikolea, A. Balducci, *Batteries* **2018**, *1*, 204–208.
- [23] H. L. Zhu, F. Zhang, J. R. Li, Y. B. Tang, *Small* **2018**, *14*, 1703951.
- [24] Y. Qi, J. Zhao, C. Yang, H. Liu, Y.-S. Hu, *Small Methods* **2018**, *2*, 1800111.
- [25] X. Cheng, D. Li, F. Liu, R. Xu, Y. Yu, *Small Methods* **2018**, *2*, 1800170.
- [26] A. Eftekhari, Z. Jian, X. Ji, *ACS Appl. Mater. Interfaces* **2016**, *9*, 4404–4419.
- [27] W. Zhang, J. Mao, S. Li, Z. Chen, Z. Guo, *J. Am. Chem. Soc.* **2017**, *139*, 3316–3319.
- [28] B. F. Ji, F. Zhang, N. Z. Wu, Y. B. Tang, *Adv. Energy Mater.* **2017**, *7*, 1700920.

- [29] K. Lei, C. Wang, L. Liu, Y. Luo, C. Mu, F. Li, J. Chen, *Angew. Chem. Int. Ed.* **2018**, *57*, 4687–4691; *Angew. Chem.* **2018**, *130*, 4777–4781.
- [30] B. F. Ji, F. Zhang, X. H. Song, Y. B. Tang, *Adv. Mater.* **2017**, *29*, 1700519.
- [31] M.-C. Lin, M. Gong, B. Lu, Y. Wu, D.-Y. Wang, M. Guan, M. Angell, C. Chen, J. Yang, B.-J. Hwang, H. Dai, *Nature* **2015**, *520*, 324–328.
- [32] Q. Zhang, L. Wang, J. Wang, C. Xing, J. Ge, L. Fan, Z. Liu, X. Lu, M. Wu, X. Yu, H. Zhang, B. Lu, *Energy Storage Mater.* **2018**, *15*, 361–367.
- [33] J. A. Read, A. V. Cresce, M. H. Ervin, K. Xu, *Energy Environ. Sci.* **2014**, *7*, 617–620.
- [34] S. Rothermel, P. Meister, G. Schmuelling, O. Fromm, H.-W. Meyer, S. Nowak, M. Winter, T. Placke, *Energy Environ. Sci.* **2014**, *7*, 3412–3423.
- [35] X. Zhang, F. Zhang, Y. B. Tang, C.-S. Lee, *Adv. Energy Mater.* **2016**, *6*, 1502588.
- [36] X. Shi, W. Zhang, J. Wang, W. Zheng, K. Huang, H. Zhang, S. Feng, H. Chen, *Adv. Energy Mater.* **2016**, *6*, 1601378.
- [37] M. Wang, C. L. Jiang, S. Q. Zhang, X. H. Song, Y. B. Tang, H. M. Cheng, *Nat. Chem.* **2018**, *10*, 667–672.
- [38] G. Wang, M. Yu, J. Wang, D. Li, D. Tan, M. Löffler, X. Zhuang, K. Müllen, X. Feng, *Adv. Mater.* **2018**, *30*, 1800533.
- [39] L. Fan, Q. Liu, S. Chen, Z. Xu, B. Lu, *Adv. Energy Mater.* **2017**, *7*, 1602778.
- [40] S. Wang, S. Jiao, D. Tian, H.-S. Chen, H. Jiao, J. Tu, Y. Liu, D.-N. Fang, *Adv. Mater.* **2017**, *29*, 1606349.
- [41] M. Wang, Y. B. Tang, *Adv. Energy Mater.* **2018**, *8*, 1703320.
- [42] P. P. Qin, M. Wang, N. Li, H. L. Zhu, X. Ding, Y. B. Tang, *Adv. Mater.* **2017**, *29*, 1606805.
- [43] S. Q. Zhang, M. Wang, Z. M. Zhou, Y. B. Tang, *Adv. Funct. Mater.* **2017**, *27*, 1703035.
- [44] C. Cui, Z. Wei, J. Xu, Y. Zhang, S. Liu, H. Liu, M. Mao, S. Wang, J. Ma, S. Dou, *Energy Storage Mater.* **2018**, *15*, 22–30.
- [45] C. L. Jiang, Y. Fang, J. H. Lang, Y. B. Tang, *Adv. Energy Mater.* **2017**, *7*, 1700913.
- [46] T. Placke, A. Heckmann, R. Schmuck, P. Meister, K. Beltrop, M. Winter, *Joule* **2018**, *2*, 1–23.
- [47] M. Armand, J.-M. Tarascon, *Nature* **2008**, *451*, 652–657.
- [48] H. Zhang, X. Zhang, Y. Ma, *Electrochim. Acta* **2015**, *184*, 347–355.
- [49] F. Zhang, B. F. Ji, X. F. Tong, M. H. Sheng, X. L. Zhang, C. S. Lee, Y. B. Tang, *Adv. Mater. Interfaces* **2016**, *3*, 1600605.
- [50] H. J. Liao, Y. M. Chen, Y. T. Kao, J. Y. An, Y. H. Lai, D. Y. Wang, *J. Phys. Chem. C* **2017**, *121*, 24463–24469.
- [51] N. Gunawardhana, Y. Ogumori, M. Yoshio, H. Nakamura, *Int. J. Electrochem. Sci.* **2014**, *9*, 6975–6984.
- [52] L. J. Hardwick, M. Hahn, P. Ruch, M. Holzapfel, W. Scheifele, H. Buqa, F. Krumeich, P. Novák, R. Kötz, *Electrochim. Acta* **2006**, *52*, 675–680.
- [53] N. Li, F. Zhang, Y. B. Tang, *J. Mater. Chem. A* **2018**, *6*, 17889–17895.
- [54] Y. Zhu, L. Peng, D. Chen, G. Yu, *Nano Lett.* **2015**, *16*, 742–747.
- [55] H. Shang, Z. Zuo, L. Li, F. Wang, H. Liu, Y. Li, Y. Li, *Angew. Chem. Int. Ed.* **2018**, *57*, 774–778; *Angew. Chem.* **2018**, *130*, 782–786.
- [56] P. Simon, Y. Gogotsi, *Nat. Mater.* **2008**, *7*, 845–854.
- [57] B. Babu, P. G. Lashmi, M. M. Shajumon, *Electrochim. Acta* **2016**, *211*, 289–296.
- [58] X. Sun, X. Zhang, H. Zhang, N. Xu, K. Wang, Y. Ma, *J. Power Sources* **2014**, *270*, 318–325.
- [59] J. Come, V. Augustyn, J. W. Kim, P. Rozier, P.-L. Taberna, P. Gogotsi, J. W. Long, B. Dunn, P. Simon, *J. Electrochem. Soc.* **2014**, *161*, A718–A725.
- [60] F. Wang, C. Wang, Y. Zhao, Z. Liu, Z. Chang, L. Fu, Y. Zhu, Y. Wu, D. Zhao, *Small* **2016**, *12*, 6207–6213.
- [61] H. Wang, C. Guan, X. Wang, H. J. Fan, *Small* **2015**, *11*, 1470–1477.

Manuscript received: December 5, 2018

Revised manuscript received: January 8, 2019

Accepted manuscript online: January 12, 2019

Version of record online: February 28, 2019